1-25-2022

Elucidating the Mass Transfer Mechanism of CrVI Adsorption by Encapsulated Chitosan-Carbon Nanotubes-Iron Beads in Packed-Bed Columns

Mian Muhammad Ahson Aslam

Walter Den

Hsion-Wen Kuo

Elucidating the Mass Transfer Mechanism of Cr^{VI} Adsorption by Encapsulated Chitosan-Carbon Nanotubes-Iron Beads in Packed-Bed Columns

Mian Muhammad Ahson Aslam[1], Walter Den[2,*], Hsion-Wen Kuo[1]

[1] Department of Environmental Science and Engineering, Tunghai University, No. 1727, Section 4, Taiwan Boulevard, Xitun District, Taichung City, 407, Taiwan, R.O.C.

[2] Institute for Water Resources Science and Technology, Department of Mathematical, Physical and Engineering Sciences, Texas A&M University-San Antonio One University Way, San Antonio, Texas, 78224, U.S.A.

* Author to whom all correspondence should be addressed.

Abstract

This study evaluates the Cr^{VI} breakthrough behaviors of a continuous-flow column packed with composite chitosan-MWCNTs-iron beads under various operating conditions. Under the tested range of experimental parameters, a maximum of 54% of Cr^{VI} removal was achieved at: water flow rate, 1 mL/min, feed Cr^{VI} concentration, 30 mg/L; and packed bed height 8 cm. A homogeneous surface diffusion model (HSDM) involving convection-dispersion and diffusion equations was formulated, numerically solved, and experimentally validated. The high degree of conformity between the calculated and experimental breakthrough curves also facilitated the determination of the mass transfer parameters including axial dispersion D_L, (1.30×10^{-8} to 1.56×10^{-7} m^2/s) and surface diffusion D_s, (7.28×10^{-11} to 1.80×10^{-10} m^2/s) via an error minimizing approach. The D_L value was a function of molecular diffusion, which varied with the flow velocity, mass loading, and bed height. The D_s values were slightly higher than those previously reported, owing to the heterogeneous nature of the adsorbent. The external film diffusion coefficient (k_f) was also determined by using Wilson-Geankoplis empirical correlation, which was recognized as a rate-controlling factor during Cr^{VI} mass transfer to the adsorbent beads. Furthermore, sensitivity analysis showed that a transition from diffuse- to shock-front occurred with a decreasing D_L, while a decrease in the slope of breakthrough curves was observed by decreasing D_s and bed porosity, and increasing k_f and Langmuir parameters. Lastly, the study demonstrated a high correlation between utilization of fractional bed capacity and axial Peclet number. This method is suitable for optimizing operating conditions to maximize the utilization of a fixed-bed columns.

37 Keyword: Chitosan, MWCNTs, hexavalent chromium, fixed-bed adsorption, HSDM, axial
38 dispersion, surface diffusion, COMSOL

1. Introduction

To date, activated carbon adsorption remains the most widely used method for removing toxic heavy metal ions from impaired water due to its reliability, operational versatility, and low cost [1]. The development of convection-dispersion-diffusion models has markedly facilitated the design and prediction of field-scale packed-bed systems loaded with activated carbon and other materials with high specific surface area [2,3]. In a dynamic adsorption process, a continuous solute flow passes through a column packed with specific adsorbents. A breakthrough curve for the column adsorption process can be calculated from the ratio of metal ions concentrations at outflow and inflow of the column as a function of time. The higher specific surface area, often combined with appropriate surface charges, generally allows such systems to capture heavy metal ions effectively. The microporous characteristic of these materials generating their high surface area is also responsible for the rate-limiting mass transfer of molecules once they reach the solid surface. Such mass transfer phenomenon has been conceptually and mathematically described by film transfer, surface diffusion, and pore diffusion. Incorporating the various mass transfer mechanisms into the convection-dispersion-diffusion models has proven effective in delineating the packed-bed column breakthrough behaviors [4–9].

The recent material advances trend towards modifying functional components by crosslinking and grafting to improve both adsorption performance and regeneration. Such engineered composite materials aim to either increase adsorption sites or to be selective to a specific contaminant in water matrices when tested either in batch or continuous process. For instance, researchers have identified several types of materials for uptake of Cr and other heavy metal ions with excellent selectivity, high uptake capacity and fast adsorption kinetics at low

concentrations of metal ions. These materials includes chitosan flakes [10], cross linked chitosan-iron(III) composite [11] iron decorated MWCNTs modified with chitosan film [12], Chitosan coated carboxylic-MWCNTs [13], chitosan modified magnetic graphene oxide [14], MWCNTs grafted with polypropylene-amine [15], amino functionalized graphene oxide [16], tailor made polymer nanoparticles [17], and mesoporous silica functionalized with thiol group [18]. The sorbent materials mentioned above have demonstrated excellent adsorption performances. However, these studies lack the rigor to provide an in-depth analysis of detailed adsorption and mass transfer mechanisms, and so their results can only be used for case-specific projections.

Recently, our research group prepared an encapsulated chitosan-modified, iron oxide-carbon nanotubes (CS/MWCNTs/Fe) beads for the uptake of aqueous phase Cr^{VI}, the more toxic and mobile state of chromium ions as compared to Cr^{III} [19,20]. The beads were characterized by using field emission scanning electron microscope (FE-SEM) coupled energy dispersive spectrometer (EDS) for morphological topography and elemental mapping, Fourier-Transform infrared (FTIR), powder X-ray diffractometer (XRD), and X-ray photoelectron spectroscopy (XPS) for physical and chemical properties, and thermogravimetric and differential thermal analysis (TGA and DTA) for thermal stability of the beads. These "beads" exhibited the following properties: density, 1.38 g/cm^3; average diameter, 1.0 mm; pH_{PZC}, 5.0 (indicating the acid nature of its surface that would be positively charged if $pH < pH_{PZC}$), maximum Cr^{VI} adsorption capacity, 119 mg/g at pH 4.0; and 80% of Cr^{VI} removal efficiency after five cycles of adsorption-desorption process. The beads also exhibited good stability within the pH range of ~1 to ~9 where marginal weight loss was observed. The presence of MWCNTs offered enhanced porosity, surface area, and supporting functional groups (hydroxyl and carboxyl groups). The electrostatic interactions and the complexation between Cr^{VI} ions and amine groups incorporated in chitosan (CS) worked

synergistically in the CS/MWCNTs/Fe beads. Further confirmed by XPS analysis, the evolution of Cr^{III} indicates a possible charge transfer effect of Fe^{II} and/or Fe^{III} mediated through conductive carbon nanotubes, leading to the reduction of Cr^{VI} ions [19]. We further performed packed-bed column studies and fitted the breakthrough data with various empirical, one-phase resistance models such as the Thomas, Yoon-Nelson, and Adams-Bohart models. While these empirical models fitted well with the experimental data and provided first-level information on the adsorption rate, removal capacity, and service time of the adsorbent bed, they are highly case-specific and only account for global mass transfer. In addition, packed bed column process showed a selective adsorption of Cr^{VI} ions in the presence of Cu^{II}, Cd^{II} and PO_4^{3-} [20] (see Fig. S1 for removal mechanism).

Considering the heterogeneous nature of the composite materials for heavy metal ion adsorption, one has to hypothesize that the underlying mass transfer steps differ from those well-established for homogeneous, microporous activated carbon. Therefore, this study aims to elucidate the mass transfer mechanisms involved in packed-bed columns loaded with CS/MWCNTs/Fe beads to uptake Cr^{VI} from synthetic solutions. Specific objectives are: (i) To apply the convection-dispersion-diffusion model determining the rate-limiting mass transport steps, including axial dispersion, external mass transfer, intraparticle diffusion limitations, and velocity variations along the fixed-bed column. Specifically, we hypothesize that the homogeneous surface diffusion (HSDM) model would best describe the mass transfer process in this application. (ii) To validate the model using experimentally derived Cr^{VI} breakthrough curves under the influence of flow rate, feed Cr^{VI} concentration, and bed height by optimizing major design parameters such as the axial dispersion and surface diffusion coefficients. (iii) To

optimize the column operation by correlating utilization of fractional bed capacity (F_{BCU}) and axial Peclet numbers (Pe_{ax}) at varying experimental conditions.

2. Materials and Methods

2.1 Column breakthrough studies

A glass column with an internal diameter of 2 cm and a length of 14 cm was used to conduct continuous adsorption tests under the following experimental conditions: volumetric flow rate, 1, 2, 3, and 4 mL/min; bed height, 4, 6, and 8 cm; inlet Cr^{VI} concentration, 30, 50, and 100 mg/L. The columns were packed with the CS/MWCNTs/Fe composite beads, whose preparation method, material characteristics, and adsorptive capacity were reported in our previous study [19,20]. Throughout these experiments, the optimized pH value of 4 was maintained, as this was the pH value achieving the optimal equilibrium adsorption capacity for Cr^{VI} [19]. After packing with the CS/MWCNTs/Fe beads to a prescribed height, the Cr^{VI} solution of predetermined concentrations and pH were fed to the column using a peristaltic pump (EYELA MP-2000, Japan) with specified flow rates in the downward direction. The influent and effluent samples collected were analyzed for residual Cr^{VI} ions using a spectrophotometer (T60UV-Visible Spectrophotometer, U.K.) at the wavelength of 540 nm, with diphenylcarbazide as a colorimetric reagent [20].

The performance of the fixed-bed column can be evaluated in terms of breakthrough behavior, determined by plotting C_t/C_0 (ratio of outlet to inlet concentration) against time *t*. Here, Eq. 1 sets out the expression for percent removal of Cr^{VI} ions by the adsorption column:

$$R\ (\%) = \left(\frac{q_{total}}{m_{total}}\right) \times 100\% \qquad \text{Eq. 1}$$

where, q_{total} (mg) and m_{total} (mg) are the amount of total Cr^{VI} ions adsorbed in the column and that passed through the column, respectively. They can be determined using the following equations:

$$q_{total} = \frac{Q_v}{1000}\int_{t=0}^{t=t_{total}}(C_0 - C_t)\,dt \qquad \text{Eq. 2}$$

$$m_{total} = \frac{C_0 Q_v t_{total}}{1000} \qquad \text{Eq. 3}$$

where Q_v is the volumetric flow rate (mL/min), C_0 (mg/L) is the influent concentration, and t_{total} (min) is the total operating time of the column. Other experimental parameters are breakthrough time (t_b) and saturation time (t_s), herein defined as the time required to reach C_t/C_0 of 0.05 and 0.95, respectively.

2.2 Model conceptualization and formulation

Fig. 1 shows the graphical representation of the model and phenomenology of the adsorption process. Principally, we adopted the convection-dispersion equation, coupled with diffusion and adsorption inside the particles, to depict the governing mass transport dynamics of the fixed-column mathematically. The equation accounts for the effects of key operational parameters such as the superficial flow velocity, bed height, feed concentration, and packing porosity. Furthermore, we conceptualized that surface diffusion dominates the intraparticle mass transfer considering the low particle void fraction exhibited by the CS/MWCNTs/Fe composite particles. This hypothesis is driven by the particle characteristics with predominantly micropores distributed across a particle, where Cr^{VI} is captured by the rich amine and hydroxyl functions groups of CS and MWCNTs. Pore diffusion, which occurs when molecules are migrated from the particle's interior to reach the micro-structured surfaces through the bi-disperse pore structure of the particles, can therefore be neglected. The importance of experimental parameters lies in determining the performance of the adsorbent beads in capturing Cr^{VI} ions. However, designing a

process that merely measures these parameters is inadequate, and prediction of breakthrough behavior of the effluent is needed. Mathematical models can help to explain the kinetics of fixed-bed columns and analyze the characteristics of the adsorption breakthrough curve. Modeling usually describes the mechanisms involved in the mass transfer process, and therefore, it assists in predicting the overall efficiency of the process, which in turn supports the scaling-up of the process from laboratory to pilot scale and finally to field applications.

Based on the following assumptions, the mathematical model is formulated to explain the transport and removal of Cr^{VI} in a fixed-bed column:

1. The system operates in isobaric and isothermal conditions.
2. Axial dispersion along the longitudinal axis is taken into account, and the axial flow is uniform across the cross-sectional area of the column.
3. Sphered-shaped adsorbent particles are uniform in size and density, and column void fraction remains constant during the adsorption process.
4. Surface diffusion dominates the intraparticle mass transfer where solid-liquid equilibrium is characterized by the Langmuir adsorption isotherm [19].
5. The physical properties of the adsorbents and liquid-phase remain constant.
6. The system does not undergo any chemical reaction.

By applying the liquid-phase mass balance, i.e., *Accumulation = Output - [Input + Generation due to mass transfer]*, one can express the one-dimensional convection-dispersion equation as follows:

$$\frac{\partial C_{(z,t)}}{\partial t} = D_L \frac{\partial^2 C_{(z,t)}}{\partial z^2} - V_s \frac{\partial C_{(z,t)}}{\partial t} - \frac{(1-\varepsilon_b)}{\varepsilon_b} \rho_b \frac{\partial q_{(z,t)}}{\partial t} \qquad \text{Eq. 4}$$

The last term represents the generation term, $\frac{\partial q_{(z,t)}}{\partial t}$ being the solid mass transfer rate and $\frac{\partial C_{(z,t)}}{\partial t}$ being the accumulation term in the column bed. In the equation, D_L (m^2/s) is the axial dispersion

coefficient, z (m) is the length of the longitudinal axis of the bed, V_s (m/s) is the interstitial velocity, t (h) is the time of column operation, and ε_b is the bed porosity. Furthermore, the last term in Eq. 4 is related to the mass transfer of Cr^{VI} ions driven by the concentration gradient across the stagnant boundary layer of the adsorbent particle:

$$\rho_b \frac{\partial q_{(z,t)}}{\partial t} = \frac{3k_f}{R_p}\left(C_{(z,t)} - C_{((z,t,),r=R_p))}\right) \quad \text{Eq. 5}$$

where k_f (m/s) is the film mass transfer coefficient, R_p (m) is particle radius and C_s (mg/L) is the concentration of Cr^{VI} ions at the surface of adsorbent particle. Eq. 5 can be substituted into Eq. 4 to obtain:

$$\frac{\partial C_{(z,t)}}{\partial t} = D_L \frac{\partial^2 C_{(z,t)}}{\partial z^2} - V_s \frac{\partial C_{(z,t)}}{\partial t} - \frac{(1-\varepsilon_b)}{\varepsilon_b}\frac{3k_f}{R_p}\left(C_{(z,t)} - C_{s((z,t),r=R_p)}\right) \quad \text{Eq. 6}$$

The following initial and boundary conditions were applied to the column inlet and outlet:

$$C(z, t=0) = 0 \quad \text{Eq. 7a}$$

$$\frac{\partial C_{(z=0,t)}}{\partial z} = \frac{V_s(C_{(z=0,t)} - C_0)}{D_L} \quad \text{Eq. 7b}$$

$$\frac{\partial C_{(z=L,t)}}{\partial z} = 0 \quad \text{Eq. 7c}$$

The mass balance equation for concentration profiles inside the adsorbent particle accounting for surface diffusion in the radial direction is given as follows:

$$\frac{\partial q_{(r,t)}}{\partial t} = \frac{D_s}{r^2}\frac{\partial}{\partial r}\left(r^2 \frac{\partial q_{(r,t)}}{\partial r}\right) \quad \text{Eq. 8}$$

where D_s (m^2/s) is the surface diffusion coefficient and r (m) is the radial coordinate. The corresponding initial and boundary conditions are given as follows:

$$q(r, t=0) = 0 \quad \text{Eq. 9a}$$

$$\frac{\partial q}{\partial r}(r=0, t) = 0 \quad \text{Eq. 9b}$$

$$q(r > 0, t) = q_e \quad \text{Eq. 9c}$$

$$\rho_b D_s \frac{\partial q}{\partial r}\left(r = R_p, t\right) = \frac{1-\varepsilon}{\varepsilon} k_f \left(C_{(z,t)} - C_{s((z,t),r=R_p)}\right) \quad \text{Eq. 9d}$$

To describe the fluid and solid-phase equilibrium at the surface of the adsorbent particle, we used the Langmuir isotherm, expressed in Eq. 10 and computed in our previous study [19].

$$q_e = \frac{K_L\, q_{max}\, c_s}{1 + K_L\, C_s} \quad \text{Eq. 10}$$

where K_L (L/mg) and q_{max} (mg/g) are the equilibrium constant and maximum adsorption capacity, respectively.

The model equations that account for the effects of axial dispersion, film diffusion, and surface diffusion are generally referred to as the homogeneous surface diffusion model (HSDM). Previous studies have described the kinetics of fixed-bed columns by using numerical models that include external and internal mass-transfer limitations with a non-ideal plug flow ignoring axial dispersion [2,3,21–23]. Nonetheless, axial dispersion remains a crucial aspect along with the column domain. Concerning the mass transfer process, empirical correlations involving dimensionless numbers such as Reynold number (*Re*), Schmidt number (*Sc*), Sherwood number (*Sh*), and Biot number (*Bi*) are helpful for evaluating the rate-limiting steps. These dimensionless parameters are given as follows:

$$Sh = \frac{1.09}{\varepsilon_b} Re^{0.33} Sc^{0.33}, \text{ for } 0.00015 < Re < 55 \quad \text{Eq. 11}$$

where $R_e = \frac{V_s \rho_L d_p}{\mu}$ and $S_c = \frac{\mu}{D_m\, \rho_L}$, in which ρ_L (g/L) and μ (g/m·s) denote to the density and viscosity of liquid phase, respectively, D_m (m^2/s) and d_p (m) denote to the molecular diffusivity of Cr^{VI} ions and particle diameter, respectively.

The film mass transfer coefficient can be calculated using Eq. 12:

$$k_f = \frac{Sh * D_m}{d_p} \quad \text{Eq.12}$$

The breakthrough curves obtained may have a significant effect due to small variations in k_f, which gives the coefficient of sensitivity analysis. With regards to evaluating the sensitivity of film resistance, the Biot number is applied as follows:

$$Bi = \frac{k_f d_p C_0}{2 D_s \rho_p q_0} \quad \text{Eq. 13}$$

where ρ_p (kg/m^3) is particle density and q_0 is the adsorbed Cr^{VI} concentration corresponding to C_0. The Biot number determines the influence of intraparticle diffusion compared to mass transfer across a film layer. When $Bi < 1$, film diffusion dominates the adsorption rate, whereas surface diffusion is the major resistance when $Bi > 1$ [24].

Numerically solving the model equations (Eq. 4-10) allows for evaluating the mass transport parameters independently – namely the axial dispersion and surface diffusion coefficients – by fitting the simulated breakthrough curves with the corresponding experimental curves. The order of magnitude of these parameters is highly dependent on adsorption rates and flow conditions, geometric parameters such as bed height, bed porosity, and particle size of the applied adsorbent as well surface diffusivity of the adsorbate. By including the axial dispersion term, we calculated the axial Peclet number (Pe_{ax}) using Eq. 14 and correlated it with other operational parameters:

$$Pe_{\mathrm{ax}} = \frac{V_s L_c}{D_L} \quad \text{Eq. 14}$$

where L_c (m) is the characteristic length of the column.

2.3 Numerical solution of the formulated model

COMSOL Multiphysics® (COMSOL, Inc.) version 5.6 was used to solve the model equations numerically. We employed the Chemical Species Transport (CST) module for one-dimensional (for liquid phase PDE) and two-dimensional (for particle phase PDE) and time-dependent study. The COMSOL solver uses the finite element method to discretize the spatial

boundaries and adaptive meshing and error control algorithms. In the CST module, a sub-module (i.e., mass transport of diluted species through porous media) was adopted to incorporate the convection and diffusion equations within the column domain. Fig. 2 shows a flowchart of the route followed for the simulation process using COMSOL Multiphysics®.

Fig. 3 illustrates the spatial discretization scheme for implementing the model equations with corresponding initial and boundary conditions. The one-dimensional geometry of the fixed-bed column was first discretized into a set of smaller elements. To describe mass transfer by surface diffusion in the radial direction, the one-dimensional mesh was extruded to a two-dimensional mesh for a dimensionless particle radius where the rectangular spatial elements can be observed. The convection-dispersion equation was used to simulate the distribution of Cr^{VI} ions in the axial direction of the bed. In contrast, the diffusion equation was used to estimate the mass transport of Cr^{VI} ions inside the adsorbent particles. Using the convection-dispersion equation, the bulk concentration of Cr^{VI} ions and the Danckwerts boundary condition (i.e., $n \cdot (-D\nabla C + uC_{z=0}) = n \cdot uC_0$) are set at the inlet (i.e., $C = 0$) and convective influx (i.e., $n \cdot D\nabla C = 0$) at the outlet. The reaction term R was substituted for the mass transfer rate of Cr^{VI} ions at the solid-liquid interface as expressed in the last term of Eq. 6. In addition, for the diffusion equation, one can assume the following: (i) all solid phase elements were free of initial Cr^{VI} concentration (i.e., $q = 0$); (ii) the diffusive flux in the center of the particle followed symmetry (i.e., $n \cdot D\nabla q = 0$); and (iii) the diffusive flux at the outer surface followed a boundary condition in Eq. 9d (i.e., $\rho_p D_s \nabla q = \frac{1-\varepsilon_b}{\varepsilon_b} k_f (C - C_s)$).

2.4 Model validation

To validate the HSDM model, the first step was to employ the finite element algorithm solution under various experimental conditions to compute D_L and D_s by minimizing the objective function as follows:

$$\sum_1^n \left(\frac{C_{exp}}{C_0} - \frac{C_{cal}}{C_0}\right)^2 \qquad \text{Eq. 15}$$

where C_{exp} and C_{cal} (mg/L) are the experimental and calculated Cr^{VI} concentrations, respectively, at the outlet of the column, and n is the total number of observations. The degree of correlation between the computed and the experimental data was evaluated based on the values of coefficient of determination (R^2) and the sum of squared error (SSE). The D_L values computed through model fitting were compared with the various correlations reported in the literature. After validating the model, the sensitivity analysis was performed for the different parameters in model equations, including mass transfer parameters (D_L, D_s, k_f), adsorption parameters (q_{max}, K_L), and geometric parameters (ε_b). The other hydrodynamic parameters (Pe_{ax}, Re, Sc, Sh, and Bi) were not subjected to the sensitivity analysis because they depend on the mass transfer parameters and were measured from empirical correlations.

3. Results and Discussion

3.1. Model validation

Table 1 summarizes the numerical values of the key parameters evaluated in the study, including the control variables (Q_v, L, and C_0), the resulting breakthrough properties (t_b, t_s, and *% removal*), the fitted mass transfer parameters (D_L, D_s, k_f) and the corresponding dimensionless groups (Pe_{ax}, Re, Sc, Sh, and Bi). The synchrony between t_s and t_b reflects the symmetric pattern (S-shaped) of the breakthrough curves. Both t_s and t_b values markedly decrease with greater pollutant mass loadings by increasing either the flow rate or the influent concentration.

Evidently, the theory of moving mass transfer zone (MTZ) applies in this study when Cr^{VI} is introduced into a fixed-bed column, propagating the MTZ towards the column outlet at a constant velocity. The time difference between breakthrough and saturation ($t_s - t_b$), which characterizes the S-shaped zone of the breakthrough curve, decreases as the inlet Cr^{VI} concentration and flow rate increases. The higher the adsorbate concentration, the faster the adsorption sites on the adsorbent are saturated.

Fig. 4a-c show that the model and experimental results are well correlated, and that the convection-dispersion-diffusion model applies appropriately to the fixed-bed columns packed with CS/MWCNTs/Fe beads, as manifested by the high values of R^2 (0.980 to 0.997) and low SSE values (4.93×10^{-2} to 0.99×10^{-2}). The computed mass transfer parameters, namely D_L and D_s, are dependent of the experimental conditions such as flow velocity, bed height, and feed Cr^{VI} concentration. In contrast, the k_f value obtained from the empirical correlation changes only with flow velocity, suggesting that the mass transfer coefficient depends primarily on the hydrodynamic factors for specific adsorbate-adsorbent systems.

The computed D_L values range of 10^{-8} to 10^{-7} m^2/s, as indicated in Table 1. As D_L is known to be a function of the adsorbent's geometry, several theoretical correlations have been used to estimate the dispersion coefficient based on the characteristics and mass transport properties of adsorbents and adsorbates [25–31] (details can be found in Table S1). Among these correlations, Edward and Richardson [25] proposed an empirical expression for estimating D_L values relating to molecular diffusion and eddy diffusion.

$$D_L = 0.73D_m + \frac{0.5V_s d_p}{1+\frac{9.7D_m}{V_s d_p}} \text{ for } 0.008 < Re < 50 \text{ and } 0.377 < d_p < 6 \text{ mm} \qquad \text{Eq. 16}$$

This correlation assumes that molecular diffusion dominates at low *Re* values, while eddy diffusion dominates at high *Re* values. The value of D_m can be calculated from the following correlation [32]:

$$D_m = 2.74 \times 10^{-9}(M_w)^{-1/3} \quad \text{Eq. 17}$$

where M_w (g/mol) is the molecular weight of the solute. The D_m value obtained was in the order of 10^{-9} m^2/s, consistent with what has been reported in the literature [33,34]. The calculated D_L values using Edward and Richardson correlation are within the same range as those obtained by fitting experimental data using HSDM with a valid *Re* ranging from 0.020 to 0.079 (Table S1). These findings support the model's applicability for predicting the behavior of breakthrough curves and determining the mass transfer parameters in the CS/MWCNTs packed column.

The optimal value of D_s was found to be in the range of 10^{-11} to 10^{-10} m^2/s, which is slightly higher than those determined in earlier studies using the HSDM (See Table S2). The changing values of D_s with experimental conditions suggest that this parameter is weakly dependent on the fluid-solid phase loading. This result deviates from the prevailing assumption that the surface diffusion coefficient is a constant for a specific adsorbate-adsorption system. For instance, several researchers reported a constant value of D_s in their fluid-solid phase systems, whose loading conditions affected the external diffusion but not the intraparticle diffusion, with the latter identified as the rate-controlling step [24,35–43] (see Table S2 for a comparison of D_s values). The heterogeneous nature of the adsorbent particles used in this study –macro-pores on the outer alginate surfaces and meso- and micro-pores on the chitosan and carbon nanotube surfaces – may have precipitated the varying surface diffusion coefficient. We will corroborate this argument in the discussion of sensitivity analysis of D_s, section 3.2.1.

3.1.1. Breakthrough responding to varying flow rates

Fig. 4a displays the experimental and computed Cr^{VI} adsorption breakthrough profiles using varying flow rates (1, 2, 3, and 4 mL/min) and constant bed height (8 cm) and feed Cr^{VI} concentration (30 mg/L). The results indicate that mass transfer parameters such as D_L, k_f, and D_s are a function of the flow velocity. The D_L increases with flow rate due to local concentration gradients resulting from non-homogeneities in liquid phase concentrations. It is well established that, with increasing flow rates, convection-dispersion prevails over molecular diffusion [44]. However, the lower range of *Re* (0.020 to 0.079) signifies that molecular diffusion should also be notable [25]. Considering the low *Re* values applied in this study and the interrelationship between axial dispersion and molecular diffusion as described in Eq. 16, the role of axial diffusion in the column mass transfer process needs to be accounted for. At lower flow rates, molecular diffusion occurs slowly, decreasing the column's dispersion significantly, as reflected by the increase in Pe_{ax} [45] (Table 1).

The k_f value, calculated based on an empirical correlation, increases with flow rates due to the decrease in mass transfer resistance in the film layer [7]. Consequently, the increases in D_s value from 7.28×10^{-11} to 1.74×10^{-10} m^2/s corresponding to the increasing flow rates from 1 to 4 mL/min suggests that surface diffusion is not only the rate-determining step during the mass transfer process, but external film diffusion also plays a significant role. This is consistent with the implication of decreasing values of *Bi* with increasing flow rates. When its value remains less than unity, film diffusion is the major rate-controlling step during the mass transfer process, especially in the early phase of the breakthrough. Therefore, it can be deduced that, if film diffusion is the rate-determining step, the residence time decreases with increasing flow rates will result in lower Cr^{VI} removal (Table 1).

3.1.2. Breakthrough responding to varying bed heights

Fig. 4b shows the experimental and simulated breakthrough curves of Cr^{VI} adsorption over the range of 4 to 8 cm in bed height, with a constant flow rate (1 mL/min) and feed Cr^{VI} concentration (30 mg/L). The excellent agreement between the simulated and experimental breakthrough curves supports the model's suitability under varying bed heights. A greater bed height tends to increase Pe_{ax}, minimizing the axial dispersion [46]. Thus, the column gets saturated earlier with a smaller value of Pe_{ax} and the saturation time lengthens as Pe_{ax} increases, resulting in higher Cr^{VI} removal (Table 1). Conversely, the D_s value increases with decreasing bed height, indicating an increase in intraparticle resistance. This observation can be further supported by the decreasing *Bi* values with bed height, suggesting an increased film mass transfer at lower bed height.

3.1.3. Breakthrough responding to varying influent Cr^{VI} concentrations

Fig. 4c shows the adsorption and simulated breakthrough curves obtained for varying feed Cr^{VI} concentrations of 30 to 100 mg/L at a constant flow rate (1 mL/min) and bed height (8 cm). With decreasing feed Cr^{VI} concentrations (100 to 30 mg/L), the slope of the breakthrough curves decreases. This result is attributed to the smaller mass transfer flux from the bulk to the surface of the adsorbent caused by a weaker concentration gradient as the driving force in the film transfer process. Consequently, the assumption of an instantaneous equilibrium following the Langmuir isotherms holds. The increasing value of *Bi* with feed Cr^{VI} concentration also indicates a more intense mass transfer at the film layer as compared to the intraparticle mass transfer, ultimately resulting in the desorption of Cr^{VI} ions [7,24] and a decrease in Cr^{VI} removal.

3.2. Sensitivity analysis

Fig. 5a-f illustrate the sensitivity of the mass transfer and adsorption parameters included in the HSDM. The sensitivity analysis was performed by varying one parameter and holding others constant in each simulation. The baseline experimental conditions were: flow rate, 1 mL/min; bed height, 8 cm; and influent Cr^{VI} concentration, 30 mg/L.

3.2.1. Mass transfer parameters

Fig. 5a shows that when the D_L value was increased from 25% to 90% from its base case, t_b decreased by about 11% to 24%, and t_s increased by about 4%, resulting in diffuse solute fronts. Conversely, when the D_L value was decreased from 25% to 90%, the breakthrough curves sharpened, increasing t_b by ~12% to ~50% and shortening t_s by ~4% to ~15%. The sharpened solute front appeared due to minimum mass transfer resistance and decreasing axial dispersion, indicating the maximal utilization of bed capacity. However, diffuse fronts appeared due to significant mass transfer resistance and increasing axial dispersion, resulting in lower bed capacity utilization.

Fig. 5b shows that, when the D_s value was increased from 25% to 90% from the base value, the extent by which t_s reduced increased by about 4% to 8%. Conversely, decreasing the D_s value in the same range led to a significant decrease in the slope of the breakthrough curves and the increase in corresponding t_s value. However, altering D_s from the base case did not affect the breakthrough time. This result clearly distinguishes the mass transfer process between the applied composite beads and other well-established adsorbent materials. For instance, some researchers determined that altering the D_s values from its base value significantly affected the breakthrough point of the curve [3,47], while some showed otherwise and treated surface diffusion as a constant irrespective of experimental conditions [7,24,48]. This study determines that, with a varying t_s value but relatively constant t_b value, the initial phase of the breakthrough

curve experiences minimal surface diffusion resistance. In contrast, film diffusion at the external boundary layer is a critical rate-limiting step. This result is consistent with the sensitivity of k_f; when its value increased from 25% to 90%, the incipient t_b also increased by ~12% (Fig. 5c). Furthermore, we observed that the slope of the curve exhibited a negative correlation with k_f (i.e., the slope decreased with increasing k_f and vice versa). This result revealed that the mass transport was mainly governed by intraparticle diffusion in the latter part of the breakthrough curve, while k_f controlled the initial breakthrough point.

3.2.2. Adsorption parameters

Fig. 5d and 5e show the sensitivity of the maximum adsorption capacity (q_{max}) and the Langmuir constant (K_L). Increasing either of the two parameters by an extent from 25% to 90% of their base values resulted in a change of t_s by ~3% to ~7%, while t_b remained unchanged. Contrarily, decreasing the values of these parameters resulted in decreasing t_b and t_s by ~12% and ~15%, respectively. Evidently, both q_{max} and K_L are key parameters dictating the prolonged operation of the fixed-bed columns.

Fig. 4f shows the effect of bed porosity in the column. A decrease in bed porosity resulted in a slightly prolonged breakthrough time. Presumably, lowering the bed porosity leads to an increase in the surface area within a confined space. By reducing the volume of void fraction in the bed, the Cr^{VI} ions can achieve a longer contact time with the adsorbent particle and result in a longer saturation time.

3.3 Utilization of fractional bed capacity

Fig. 6a-h illustrate the iso-concentration contours of Cr^{VI} along the length of the CS/MWCNTs/Fe packed adsorption columns. In these plots, the Cr^{VI} concentration near the

column inlet ($x/L \approx 0$) is equal to C_0 since this segment is quickly saturated with Cr^{VI} ions. The Cr^{VI} concentration decreases as it propagates along the column and finally reaches zero as Cr^{VI} ions are completely adsorbed. This concentration front moves along the column axis over time. Notably, one can observe the presence of diffuse Cr^{VI} concentration profiles in response to higher bed height (8 cm) and lower solute concentrations – those generated by altering either the solute mass (30 mg/L) or the flow rate (1 mL/min) (Fig. 6a). The slope of the concentration profiles further decreased with increasing feed Cr^{VI} concentration and flow rate and decreasing bed height (Fig. 6b-h). Additionally, each of the concentration profiles travels a different distance in the column during the same interval. Eventually, the column experiences a breakthrough when Cr^{VI} ions are no longer completely adsorbed, leaving a fraction of the bed unused. For instance, at $x/L = 1$, the solute front is stopped upon reaching a concentration of 100 mg/L of Cr^{VI} ions, even though a significant fraction of the adsorbent bed has yet been fully equilibrated with the inlet concentration. Observing the area between the concentration profiles, one can identify that the amount of saturated adsorbent varies with feed concentration, flow rate, and bed height. Two indicators, namely the stoichiometric length and the MTZ of the adsorbent bed, can effectively characterize the step-function behavior of column operations. A highly efficient adsorption column should operate under optimized bed utilization by minimizing unused bed portions. We herein introduce the concept of "fractional bed capacity utilization" (F_{BCU}) given by the following expression [49]:

$$F_{BCU} = 1 - 0.5\frac{MTZ}{L} \qquad \text{Eq. 18}$$

F_{BCU} allows the column to be optimized for the time it takes to use its maximum length while avoiding the addition of extra length that would otherwise result in a sustained breakthrough. However, Cr^{VI} should be transported primarily through convection or axial

dispersion during its propagation through the utilized length. To investigate this correlation, we plotted F_{BCU} versus Pe_{ax}, as shown in Fig. 7. The column experiments performed at various flow rates, bed heights, and feed Cr^{VI} concentrations lead to the following correlations between Pe_{ax} and F_{BCU}:

$$F_{BCU} = 0.0011Pe_{ax} + 0.5306 \quad \text{for} \quad 17.8 \leq Pe_{ax} \leq 119.8 \qquad \text{Eq. 19a}$$

$$F_{BCU} = 0.0008Pe_{ax} + 0.5713 \quad \text{for} \quad 20.0 \leq Pe_{ax} \leq 119.8 \qquad \text{Eq. 19b}$$

$$F_{BCU} = 0.0011Pe_{ax} + 0.5362 \quad \text{for} \quad 7.3 \leq Pe_{ax} \leq 119.8 \qquad \text{Eq. 19c}$$

The experiments performed at a low flow rate (low *Re*) resulted in superior column utilization (high F_{BCU}). The trend accurately reflected a transition from 1 to 4 mL/min (*Re* from 0.020 to 0.079) in which an increase in *Re* correlated linearly with a reduction in the value of Pe_{ax} and F_{BCU} (Eq. 19a). The correlation between F_{BCU} and Pe_{ax} under the influence of varying bed height is given in Eq. 19b. Due to the significant effect of axial dispersion, F_{BCU} decreases with decreasing bed height, which results in a linear decrease in Pe_{ax} as discussed previously. Eq. 19c shows the correlation between F_{BCU} and Pe_{ax} under the influence of feed Cr^{VI} concentration. With an increasing feed Cr^{VI} concentration from 30 to 100 mg/L, almost the same portion of F_{BCU} was accounted for in the case of increasing flow rate and decreasing bed height. Additionally, F_{BCU} increases with decreasing the feed Cr^{VI} concentration from 100 to 30 mg/L. Increasing the concentration from 30 to 100 mg/L resulted in a reduced Pe_{ax} and an increased inactive zone in the column (smaller F_{BCU}). We concluded that having high values of F_{BCU} is beneficial to reduce the unused-bed, which can be achieved by either lowering the flow rate or the feed Cr^{VI} concentration, combined with increasing the bed height of the column.

4. Conclusions

The HSDM model was successfully validated with the experimental breakthrough data of CS/MWCNTs/Fe beads for Cr^{VI} removal from the aqueous solution in fixed-bed columns. By minimizing the objective function between the experimental and calculated breakthrough profiles, the model also allowed the determination of key mass transfer parameters, including those describing axial dispersion, surface diffusion, and film transfer, under the influence of flow rates, bed height, and feed Cr^{VI} concentrations. The resulting axial dispersion coefficient varied in the range between 10^{-8} and 10^{-7} m^2/s and the diffusion coefficient in the range between 10^{-11} and 10^{-10} m^2/s. Both ranges agreed well with those reported in the literature and were a function of the hydrodynamic conditions depicted by the dimensionless Pe_{ax}. The external film diffusion was deemed a rate-limiting step in the initial part of a breakthrough, whereas surface diffusion plays a prominent role in the latter part of the breakthrough. We further introduced the method of utilization of fractional bed capacity, whose correlation with Pe_{ax} can characterize the bed utilization efficiency. Low flow rates, low feed Cr^{VI} concentrations, and deeper bed heights improved the column adsorption efficiency.

References

[1] M. Mariana, A.K. Abdul, E.M. Mistar, E.B. Yahya, T. Alfatah, M. Danish, M. Amayreh, Recent advances in activated carbon modification techniques for enhanced heavy metal adsorption, J. Water Process Eng. 43 (2021) 102221. https://doi.org/10.1016/j.jwpe.2021.102221.

[2] A. Piazzoli, M. Antonelli, Application of the Homogeneous Surface Diffusion Model for the prediction of the breakthrough in full-scale GAC filters fed on groundwater, Process Saf. Environ. Prot. 117 (2018) 286–295. https://doi.org/10.1016/j.psep.2018.04.027.

[3] A. Ma, A. Abushaikha, S.J. Allen, G. McKay, Ion exchange homogeneous surface diffusion modelling by binary site resin for the removal of nickel ions from wastewater in fixed beds, Chem. Eng. J. 358 (2019) 1–10. https://doi.org/10.1016/j.cej.2018.09.135.

[4] M.E. Jarvie, D.W. Hand, S. Bhuvendralingam, J.C. Crittenden, D.R. Hokanson, Simulating the performance of fixed-bed granular activated carbon adsorbers: Removal of synthetic organic chemicals in the presence of background organic matter, Water Res. 39 (2005) 2407–2421. https://doi.org/10.1016/j.watres.2005.04.023.

[5] M. Usman, M. Zarebanadkouki, M. Waseem, I.A. Katsoyiannis, M. Ernst, Mathematical modeling of arsenic(V) adsorption onto iron oxyhydroxides in an adsorption-submerged membrane hybrid system, J. Hazard. Mater. 400 (2020) 123221. https://doi.org/10.1016/j.jhazmat.2020.123221.

[6] R.K. Chakravorti, T.W. Weber, Pore and Solid Diffusion Models for fixed-bed adsorbers, AIChE J. 20 (1974).

[7] M. Kavand, E. Fakoor, S. Mahzoon, M. Soleimani, An improved film–pore–surface diffusion model in the fixed-bed column adsorption for heavy metal ions: Single and multi-component systems, Process Saf. Environ. Prot. 113 (2018) 330–342. https://doi.org/10.1016/j.psep.2017.11.009.

[8] Z. Xu, J.G. Cai, B.C. Pan, Mathematically modeling fixed-bed adsorption in aqueous systems, J. Zhejiang Univ. Sci. A. 14 (2013) 155–176. https://doi.org/10.1631/jzus.A1300029.

[9] D.C.K. Ko, J.F. Porter, G. McKay, Film-pore diffusion model for the fixed-bed sorption of copper and cadmium ions onto bone char, Water Res. 35 (2001) 3876–3886. https://doi.org/10.1016/S0043-1354(01)00114-2.

[10] J.B. Dima, M. Ferrari, N. Zaritzky, Mathematical Modeling of Fixed-Bed Columns Adsorption: Hexavalent Chromium onto Chitosan Flakes, Ind. Eng. Chem. Res. 59 (2020) 15378–15386. https://doi.org/10.1021/acs.iecr.0c02004.

[11] C.A. Demarchi, A. Debrassi, J.D. Magro, N. Nedelko, A. Ślawska-Waniewska, P. Dłużewski, J.-M. Greneche, C.A. Rodrigues, Adsorption of Cr(VI) on crosslinked chitosan–Fe(III) complex in fixed-bed systems, J. Water Process Eng. 7 (2015) 141–152. https://doi.org/https://doi.org/10.1016/j.jwpe.2015.05.003.

[12] J. de O. Marques Neto, C.R. Bellato, D. de C. Silva, Iron oxide/carbon nanotubes/chitosan

magnetic composite film for chromium species removal, Chemosphere. 218 (2019) 391–401. https://doi.org/https://doi.org/10.1016/j.chemosphere.2018.11.080.

[13] Y. Huang, X. Lee, F.C. Macazo, M. Grattieri, R. Cai, S.D. Minteer, Fast and efficient removal of chromium (VI) anionic species by a reusable chitosan-modified multi-walled carbon nanotube composite, Chem. Eng. J. 339 (2018) 259–267. https://doi.org/https://doi.org/10.1016/j.cej.2018.01.133.

[14] N. Subedi, A. Lähde, E. Abu-Danso, J. Iqbal, A. Bhatnagar, A comparative study of magnetic chitosan (Chi@Fe3O4) and graphene oxide modified magnetic chitosan (Chi@Fe3O4GO) nanocomposites for efficient removal of Cr(VI) from water, Int. J. Biol. Macromol. 137 (2019) 948–959. https://doi.org/https://doi.org/10.1016/j.ijbiomac.2019.06.151.

[15] M. Behbahani, T. Gorji, M. Mahyari, M. Salarian, A. Bagheri, A. Shaabani, Application of Polypropylene Amine Dendrimers (POPAM)-Grafted MWCNTs Hybrid Materials as a New Sorbent for Solid-Phase Extraction and Trace Determination of Gold(III) and Palladium(II) in Food and Environmental Samples, Food Anal. Methods. 7 (2014) 957–966. https://doi.org/10.1007/s12161-013-9698-1.

[16] M. Behbahani, N.A.G. Tapeh, M. Mahyari, A.R. Pourali, B.G. Amin, A. Shaabani, Monitoring of trace amounts of heavy metals in different food and water samples by flame atomic absorption spectrophotometer after preconcentration by amine-functionalized graphene nanosheet, Environ. Monit. Assess. 186 (2014) 7245–7257. https://doi.org/10.1007/s10661-014-3924-1.

[17] S. Parvizi, M. Behbahani, F. Zeraatpisheh, A. Esrafili, Preconcentration and ultra-trace determination of hexavalent chromium ions using tailor-made polymer nanoparticles coupled with graphite furnace atomic absorption spectrometry: Ultrasonic assisted-dispersive solid-phase extraction, New J. Chem. 42 (2018) 10357–10365. https://doi.org/10.1039/c8nj01608a.

[18] S. Bagheri, M.M. Amini, M. Behbahani, G. Rabiee, Low cost thiol-functionalized mesoporous silica, KIT-6-SH, as a useful adsorbent for cadmium ions removal: A study on the adsorption isotherms and kinetics of KIT-6-SH, Microchem. J. 145 (2019) 460–469. https://doi.org/10.1016/j.microc.2018.11.006.

[19] M.M.A. Aslam, W. Den, H.W. Kuo, Encapsulated chitosan-modified magnetic carbon nanotubes for aqueous-phase CrVI uptake, J. Water Process Eng. 40 (2021) 101793. https://doi.org/10.1016/j.jwpe.2020.101793.

[20] M.M.A. Aslam, W. Den, H.-W. Kuo, Removal of hexavalent chromium by encapsulated chitosan-modified magnetic carbon nanotubes: Fixed-bed column study and modelling, J. Water Process Eng. 42 (2021) 102143. https://doi.org/10.1016/j.jwpe.2021.102143.

[21] E. Malkoc, Y. Nuhoglu, Y. Abali, Cr(VI) adsorption by waste acorn of Quercus ithaburensis in fixed beds: Prediction of breakthrough curves, Chem. Eng. J. 119 (2006) 61–68. https://doi.org/10.1016/j.cej.2006.01.019.

[22] Z. Aksu, F. Gönen, Biosorption of phenol by immobilized activated sludge in a continuous packed bed: Prediction of breakthrough curves, Process Biochem. 39 (2004)

599–613. https://doi.org/10.1016/S0032-9592(03)00132-8.

[23] R. Murillo, T. García, E. Aylón, M.S. Callén, M. V. Navarro, J.M. López, A.M. Mastral, Adsorption of phenanthrene on activated carbons: Breakthrough curve modeling, Carbon N. Y. 42 (2004) 2009–2017. https://doi.org/10.1016/j.carbon.2004.04.001.

[24] M. Zheng, C. Xu, H. Hu, Z. Ye, X. Chen, A modified homogeneous surface diffusion model for the fixed-bed adsorption of 4,6-DMDBT on Ag-CeOx/TiO2-SiO2, RSC Adv. 6 (2016) 112899–112907. https://doi.org/10.1039/c6ra23967f.

[25] M.F. Edwards, J.F. Richardson, Gas dispersion in packed beds, Chem. Eng. Sci. 23 (1968) 109–123. https://doi.org/10.1016/0009-2509(68)87056-3.

[26] S.F. Chung, C.Y. Wen, Longitudinal dispersion of liquid flowing through fixed and fluidized beds, AIChE J. 14 (1968) 857–866. https://doi.org/10.1002/aic.690140608.

[27] N. Wakao, T. Funazkri, Effect of fluid dispersion coefficients on particle-to-fluid mass transfer coefficients in packed beds. Correlation of sherwood numbers, Chem. Eng. Sci. 33 (1978) 1375–1384. https://doi.org/10.1016/0009-2509(78)85120-3.

[28] C.L. De Ligny, The contribution of eddy diffusion and of the macroscopic mobile phase velocity profile to plate height in chromatography : A literature investigation, J. Chromatogr. A. 49 (1970) 393–401. https://doi.org/https://doi.org/10.1016/S0021-9673(00)93651-3.

[29] M. Suzuki, J.M. Smith, Axial dispersion in beds of small particles, Chem. Eng. J. 3 (1972) 256–264. https://doi.org/10.1016/0300-9467(72)85029-9.

[30] D.M. Ruthven, Principles of Adsorption and Adsorption processes, Wiley-Interscience, New York, 1984.

[31] S.O. Rastegar, T. Gu, Empirical correlations for axial dispersion coefficient and Peclet number in fixed-bed columns, J. Chromatogr. A. 1490 (2017) 133–137. https://doi.org/10.1016/j.chroma.2017.02.026.

[32] A. Polson, Some Aspects of Diffusion in Solution and a Definition of a Colloidal Particle, J. Phys. Colloid Chem. 54 (1950) 649–652. https://doi.org/10.1021/j150479a007.

[33] R. Mukherjee, P. Bhunia, S. De, Long term filtration modelling and scaling up of mixed matrix ultrafiltration hollow fiber membrane: a case study of chromium(VI) removal, J. Memb. Sci. 570–571 (2019) 204–214. https://doi.org/10.1016/j.memsci.2018.10.026.

[34] N. Iadicicco, L. Paduano, V. Vitagliano, Diffusion coefficients for the system potassium chromate-water at 25°C, J. Chem. Eng. Data. 41 (1996) 529–533. https://doi.org/10.1021/je9502861.

[35] N. Abdel-Jabbar, S. Al-Asheh, B. Hader, Modeling, parametric estimation, and sensitivity analysis for copper adsorption with moss packed-bed, Sep. Sci. Technol. 36 (2001) 2811–2833. https://doi.org/10.1081/SS-100107631.

[36] G. McKay, Solution to the homogeneous surface diffusion model for batch adsorption systems using orthogonal collocation, Chem. Eng. J. 81 (2001) 213–221.

https://doi.org/10.1016/S1385-8947(00)00191-1.

[37] G. McKay, Application of Surface Diffusion Model to the Adsorption of Dyes on Bagasse Pith, Adsorption. 4 (1998) 361–372. https://doi.org/10.1023/a:1008854304933.

[38] S. Qi, S.S. Adham, V.L. Snoeyink, B.W. Lykins, Prediction and Verification of Atrazine Adsorption by PAC, J. Environ. Eng. 120 (1994) 202–218. https://doi.org/10.1061/(asce)0733-9372(1994)120:1(202).

[39] Y. Jia, R. Wang, A.G. Fane, Hybrid PAC-submerged membrane system for trace organics removal. I. Adsorption kinetics study of PAC in a bubbled solution, Chem. Eng. J. 155 (2009) 155–160. https://doi.org/10.1016/j.cej.2009.07.032.

[40] D. Richard, M. de L. Delgado Núñez, D. Schweich, Adsorption of complex phenolic compounds on active charcoal: Breakthrough curves, Chem. Eng. J. 158 (2010) 213–219. https://doi.org/10.1016/j.cej.2009.12.044.

[41] D.C.K. Ko, J.F. Porter, G. McKay, Multicomponent mass transport model for the sorption of metal ions on bone char, AIChE J. 50 (2004) 2130–2141. https://doi.org/10.1002/aic.10186.

[42] N.E. Davila-Guzman, F.J. Cerino-Córdova, E. Soto-Regalado, M. Loredo-Cancino, J.A. Loredo-Medrano, R.B. García-Reyes, A mass transfer model for the fixed-bed adsorption of ferulic acid onto a polymeric resin: axial dispersion and intraparticle diffusion, Environ. Technol. (United Kingdom). 37 (2016) 1914–1922. https://doi.org/10.1080/09593330.2015.1135993.

[43] H. Jiang, Y. Yang, J. Yu, Application of concentration-dependent HSDM to the lithium adsorption from brine in fixed bed columns, Sep. Purif. Technol. 241 (2020) 116682. https://doi.org/10.1016/j.seppur.2020.116682.

[44] J.M.P.Q. Delgado, A critical review of dispersion in packed beds, Heat Mass Transf. Und Stoffuebertragung. 42 (2006) 279–310. https://doi.org/10.1007/s00231-005-0019-0.

[45] F.J. García-Mateos, R. Ruiz-Rosas, M.D. Marqués, L.M. Cotoruelo, J. Rodríguez-Mirasol, T. Cordero, Removal of paracetamol on biomass-derived activated carbon: Modeling the fixed bed breakthrough curves using batch adsorption experiments, Chem. Eng. J. 279 (2015) 18–30. https://doi.org/10.1016/j.cej.2015.04.144.

[46] A. Hethnawi, W. Khderat, K. Hashlamoun, A. Kanan, N.N. Nassar, Enhancing Chromium (VI) removal from synthetic and real tannery effluents by using diatomite-embedded nanopyroxene, Chemosphere. 252 (2020). https://doi.org/10.1016/j.chemosphere.2020.126523.

[47] V. Díaz-Blancas, C.G. Aguilar-Madera, J. V. Flores-Cano, R. Leyva-Ramos, E. Padilla-Ortega, R. Ocampo-Pérez, Evaluation of mass transfer mechanisms involved during the adsorption of metronidazole on granular activated carbon in fixed bed column, J. Water Process Eng. 36 (2020) 101303. https://doi.org/10.1016/j.jwpe.2020.101303.

[48] C. Bahr, M.R. Jekel, M. Kersten, Predicting the Breakthrough of Ternary Ca–Uranyl–Carbonate Species in Mineral Water Treated by a Fixed-Bed Granular Ferric Hydroxide Adsorbent, ACS ES&T Water. 1 (2021) 366–375.

https://doi.org/10.1021/acsestwater.0c00142.

[49] H. Naidu, A.P. Mathews, Linear driving force analysis of adsorption dynamics in stratified fixed-bed adsorbers, Sep. Purif. Technol. 257 (2021) 117955. https://doi.org/10.1016/j.seppur.2020.117955.

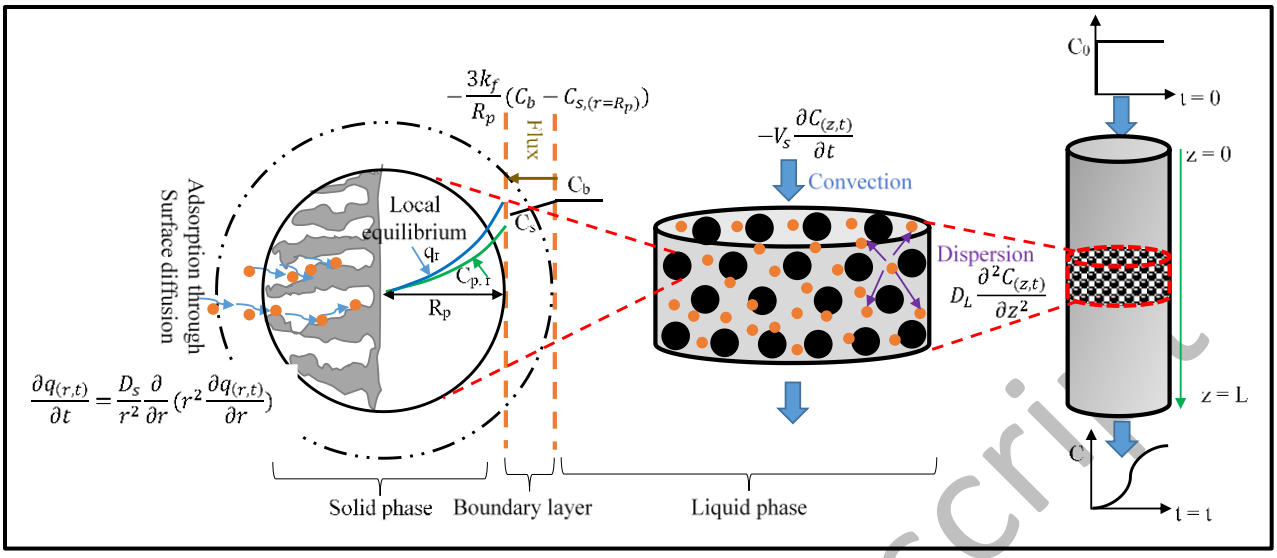

Fig. 1 Conceptual diagram of constructed model

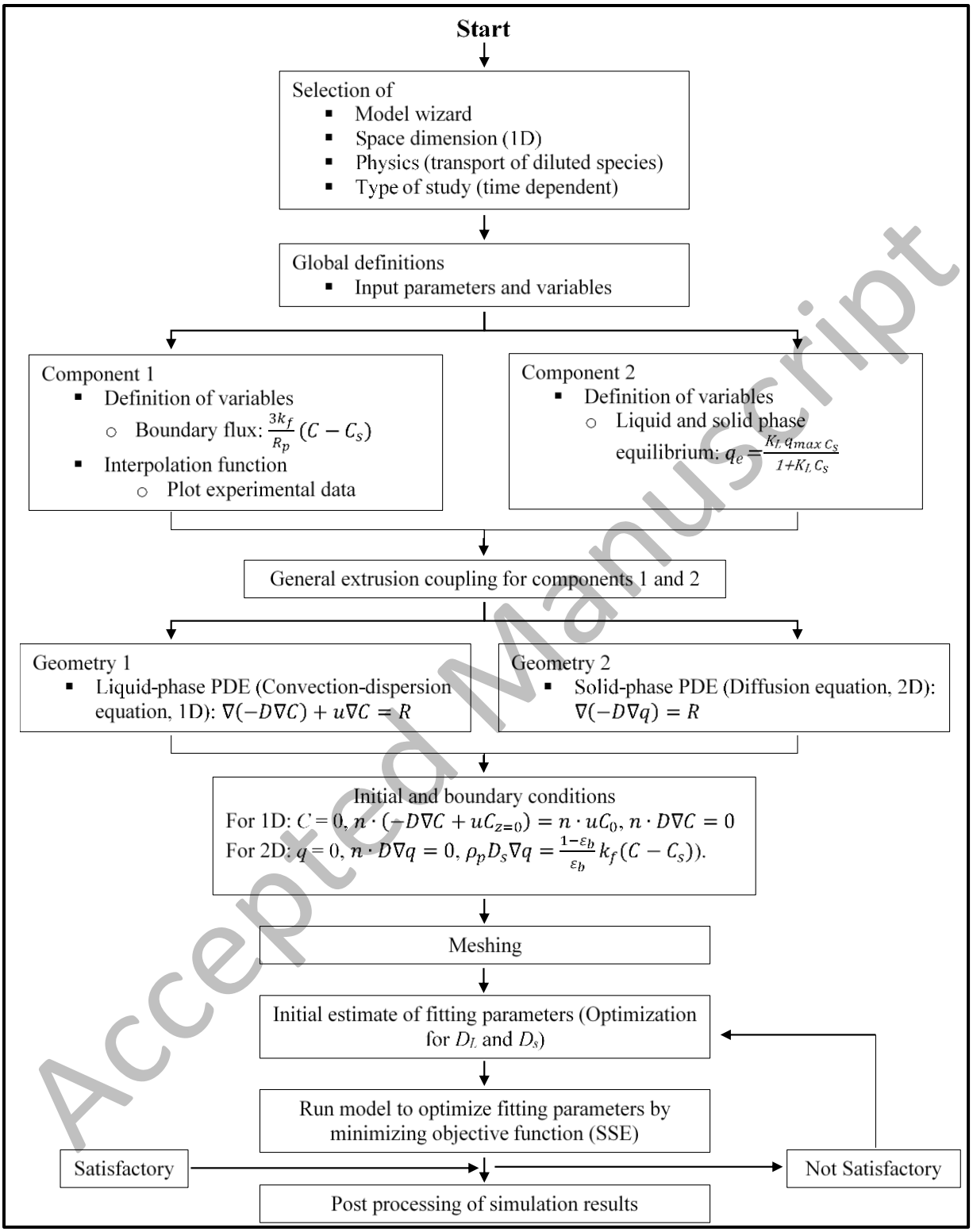

Fig. 2 Process flowchart of the route followed for the simulation process using COMSOL Multiphysics®.

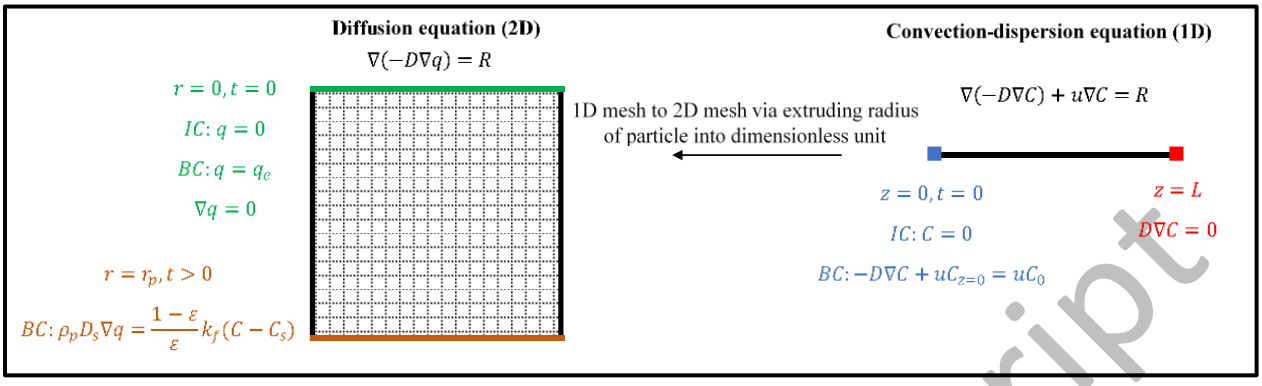

Fig. 3 Scheme of the implementation of model equations with respective initial and boundary conditions in COMSOL Multiphysics®

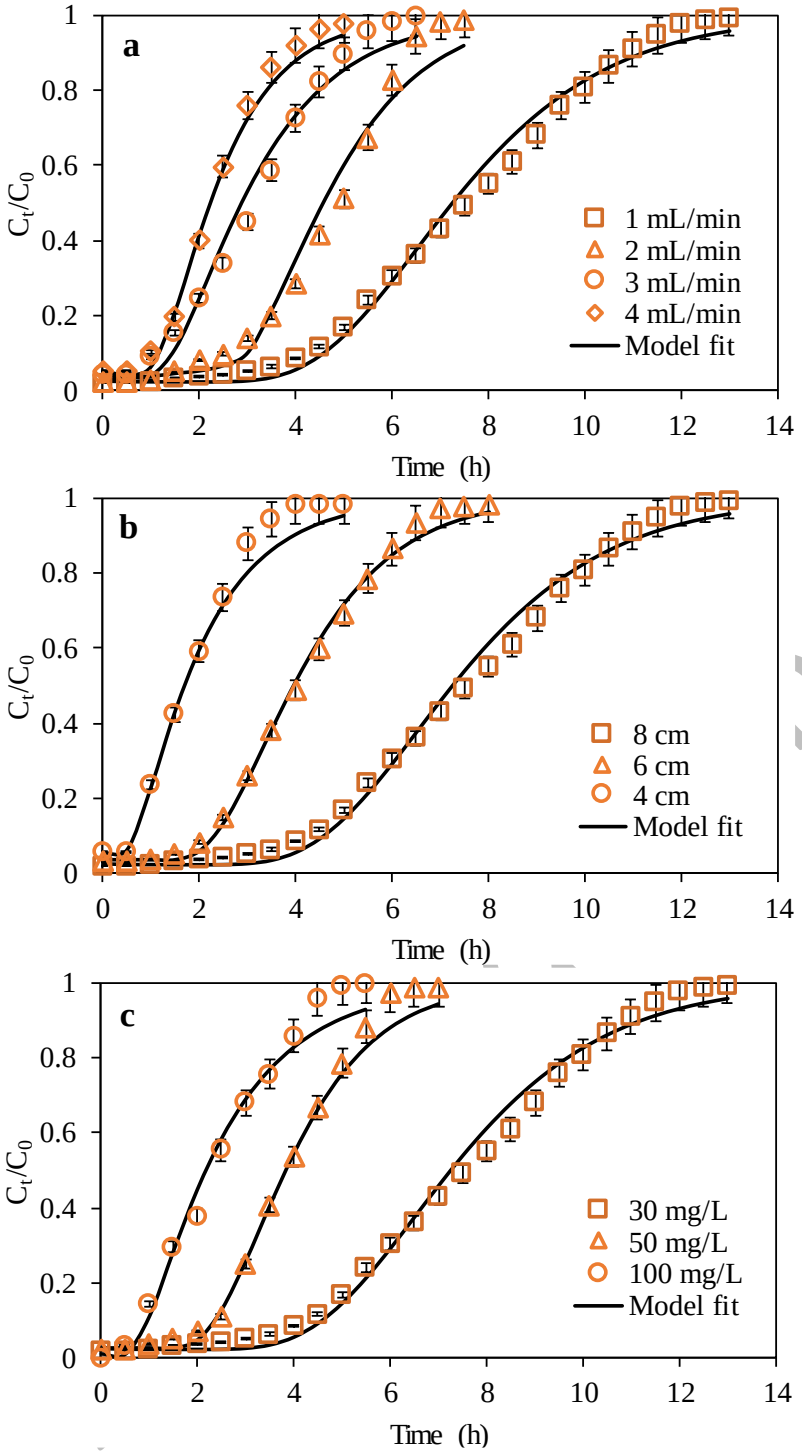

Fig. 4 Breakthrough curves of Cr^{VI} adsorption by CS/MWCNTs/Fe beads packed column at (a) varying flow rates (feed Cr^{VI} concentration, 30 mg/L; bed height, 8 cm), (b) varying bed heights (flow rate, 1 mL/min; feed Cr^{VI} concentration, 30 mg/L) and (c) varying feed Cr^{VI} concentrations (flow rate, 1 mL/min; bed depth, 8 cm). All points refer to experimental data and solid lines to HSDM model fit

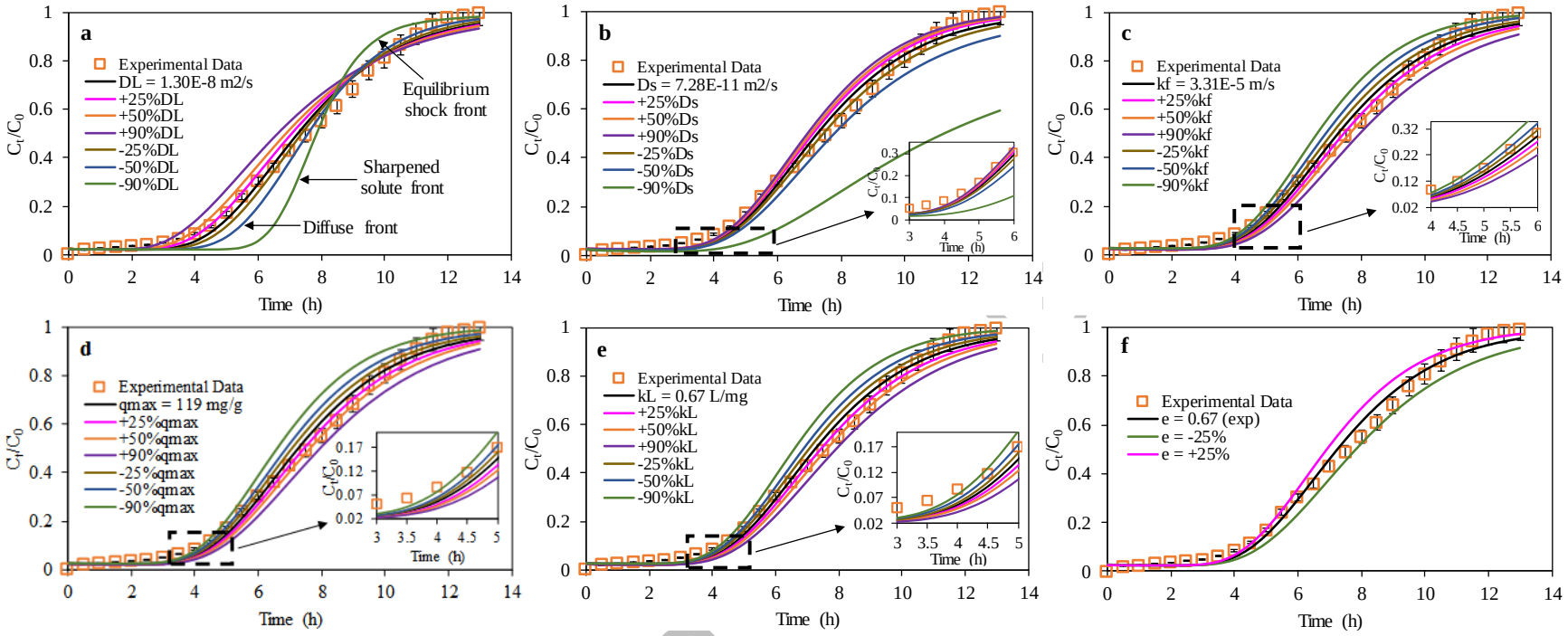

Fig. 5 Prediction and sensitivity analysis of HSDM model for (a) axial dispersion (D_L), (b) surface diffusion (D_s), (c) external film diffusion (k_f), (d) maximum Langmuir adsorption capacity (q_{max}) of the adsorbent obtained by the batch tests, (e) Langmuir constant (k_L) obtained by the batch tests and (f) bed porosity. The experimental conditions were set at flow rate, 30 mg/L; bed height, 8 cm; feed Cr^{VI} concentration 30 mg/L. The all square boxes refer to experimental data and solid line to sensitivity of HSDM for a specific parameter.

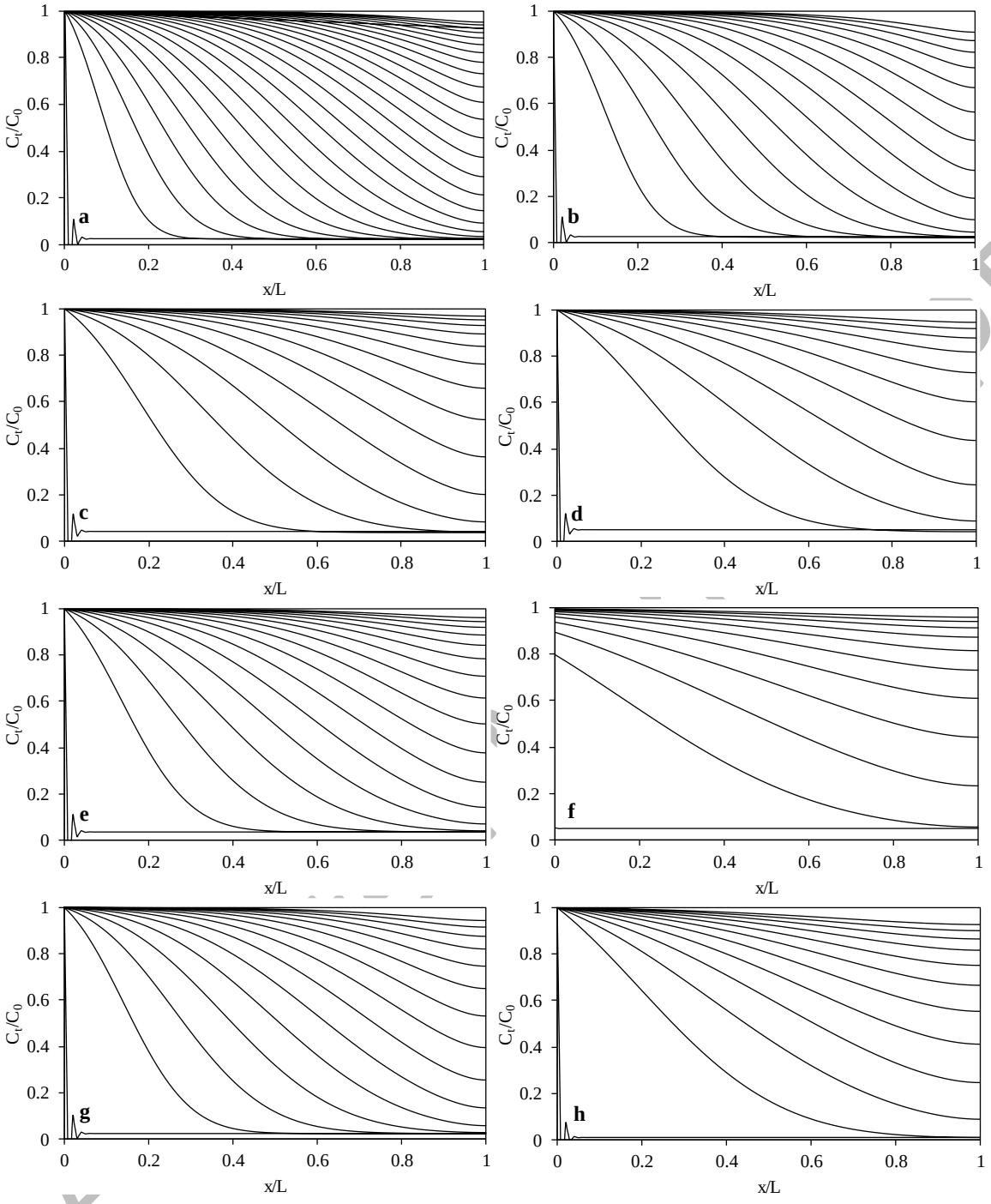

Fig. 6 Cr^{VI} concentration profiles along the CS/MWCNTs/Fe beads packed column axis at flow rates (a) 1 mL/min, (b) 2 mL/min, (c) 3 mL/min, (d) 4 mL/min at (bed height, 8 cm; feed Cr^{VI} concentration, 30 mg/L), bed heights (e) 6 cm, (f) 4 cm (flow rate 1 mL/min; feed Cr^{VI} concentration, 30 mg/L) and feed Cr^{VI} concentrations (g) 50 mg/L, (h) 100 mg/L (flow rate 1 mL/min; bed height, 8 cm)

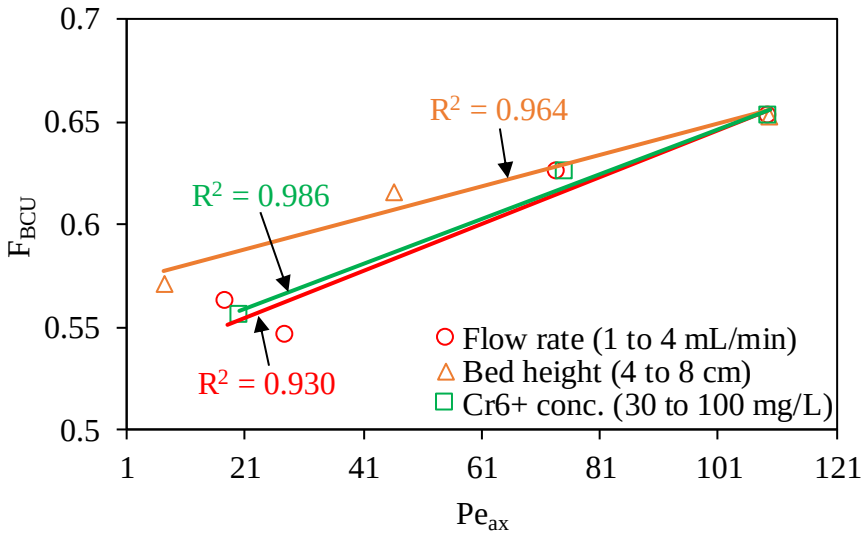

Fig. 7 Utilization of fraction bed capacity (F_{BCU}) verses axial Peclet numbers (Pe_{ax}) at varying flow rates, bed heights and feed Cr^{VI} concentrations

Table 1 Experimental and simulated parameters and mass transfer coefficients of the fixed-bed system

Q_v (ml/min)	L (cm)	C_0 (mg/L)	t_b	t_s (h)	t_s-t_b	F_{BCU}	R (%)	Re $*10^2$	Sc $*10^{-2}$	Sh	Pe_{ax}	D_L $*10^8$ (m^2/s)	D_s $*10^{10}$	K_f $*10^5$ (m/s)	Bi $*10^2$	R^2	SSE $*10^2$
1	8	30	3.5	11.5	8	0.65	53.63	1.97	1.37	2.26	109.75	1.30	0.73	3.31	4.16	0.993	2.72
2	8	30	1.5	6	4.5	0.63	55.00	3.95	1.37	2.84	73.89	1.93	1.04	4.17	3.66	0.980	4.93
3	8	30	0.5	5.5	5	0.55	40.20	5.92	1.37	3.24	27.96	5.10	1.44	4.76	3.03	0.984	3.07
4	8	30	0.5	4	3.5	0.56	36.85	7.90	1.37	3.57	17.84	7.99	1.75	5.24	2.75	0.997	0.99
1	6	30	1.5	6.5	5	0.62	45.04	1.97	1.37	2.26	75.08	1.90	1.24	3.31	2.45	0.997	0.97
1	4	30	0.5	3.5	3	0.57	27.04	1.97	1.37	2.26	20.09	7.10	1.74	3.31	1.74	0.996	2.29
1	8	50	1.5	6	4.5	0.63	48.09	1.97	1.37	2.26	46.01	3.10	1.18	3.31	4.28	0.997	2.00
1	8	100	0.5	4.5	4	0.56	35.14	1.97	1.37	2.26	7.28	15.6	1.80	3.31	5.60	0.986	2.87